

Differential RAIM and Relative RAIM for Orbit Ephemeris Fault Detection

Mathieu Joerger, Stefan Stevanovic, Samer Khanafseh and Boris Pervan
Illinois Institute of Technology
Chicago, Illinois, US
joermat@iit.edu

Abstract— This paper introduces new monitors for the detection of orbit ephemeris faults affecting differential carrier phase measurements in a shipboard aircraft landing application. Two shipboard monitors are first designed. While they provide high detection performance against two targeted fault types, they are ineffective against the other types of orbit ephemeris faults. In response, to protect the user against the entire threat space, a new airborne receiver autonomous integrity monitoring (RAIM) algorithm is developed. This ‘unified’ RAIM approach (URAIM) exploits both differential RAIM (which is most efficient at airship separation distances larger than 5 nmi) and relative RAIM (which, in contrast, performs better as the aircraft approaches the ship). Performance evaluations demonstrate URAIM’s potential to detect all types of orbit ephemeris faults using a single, unified residual-based RAIM method.

Keywords— integrity monitor; fault detection; RAIM; orbit ephemeris fault;

I. INTRODUCTION

This paper describes the design, analysis and evaluation of new shipboard and airborne monitors derived for the detection of orbit ephemeris faults. The proposed algorithms are intended for aircraft precision approach and shipboard landing applications. Prior research has shown that stringent accuracy and fault-free integrity requirements could be fulfilled using carrier phase differential GPS signals [1]. These measurements are vulnerable to rare-event faults such as satellite failures, which must be robustly detected to ensure the navigation system’s integrity.

Rare-event faults can represent a serious threat to the integrity of carrier phase differential GPS. For instance, on April 10, 2007, a GPS satellite maneuver was initiated while the satellite health flag remained set to healthy in the navigation message [2]. The satellite position error reached 700 m, which could have caused differential ranging errors to exceed several decimeters over a baseline distance (or user-to-reference separation distance) shorter than 5 km. Decimeter level errors are significant with regard to the stringent alert limit requirements specified in shipboard landing applications.

To mitigate the impact of orbit ephemeris faults, monitors used in the Local Area Augmentation System (LAAS) are first investigated. Faults caused by blundered ephemerides in the absence of spacecraft maneuvers can potentially be detected

using the LAAS Type B monitor [3], which does not require actual measurements. In contrast, LAAS monitors against faults involving a maneuver [4] cannot be used in this application. The LAAS range and range rate monitors assume a static reference antenna at an accurately known location, which is not the case of the shipboard antenna.

Therefore, in the first part of this work, we derive a new standalone shipboard monitor (SSM) which processes ionospheric-error-free code measurements using a range-comparison approach. Performance analyses show that the SSM can be efficient against faults of the same type as the April 2010 incident. Unfortunately, the SSM fails to meet the integrity risk requirement in the presence of the other types of orbit ephemeris faults, which are detailed in Sec. 2-B of this paper.

In response, a new algorithm based on receiver autonomous integrity monitoring (RAIM) is developed. It unifies two complementary methods of differential RAIM (or DRAIM) and relative RAIM (RRAIM). In DRAIM, as the aircraft approaches the ship’s reference antenna, the fault’s impact on the detection test statistic decreases. Therefore, DRAIM is most effective at the start of the aircraft approach, when the plane is far from the ship. But, its detection capability decreases as the aircraft approaches the crucial touch-down point.

As a complement to DRAIM, the RRAIM approach is developed [5]. RRAIM uses measurements that are differenced over time. The time-difference creates a synthetic baseline, which increases as the aircraft approaches the ship. As a result, the fault impact on the detection test statistic is small at the start of the approach, but it increases as the aircraft comes closer to touch-down. Therefore, DRAIM and RRAIM complement each other.

One major challenge when trying to implement RRAIM is the evaluation of the integrity risk, which is essential to determine whether an approach can be safely initiated or whether it should be aborted. This paper will show that, unlike with DRAIM, integrity risk computation using RRAIM is cumbersome. To circumvent this issue, RRAIM is implemented in conjunction with DRAIM.

DRAIM and RRAIM are combined in a unified RAIM (URAIM) algorithm. The weighted least-squares residual-

The authors gratefully acknowledge the Naval Air Systems Command (NAVAIR) of the US Navy for supporting this research. However, the opinions expressed in this paper do not necessarily represent those of any other organization or person.

based URAIM method is based on a single measurement equation. This equation is used both for state estimation and for residual generation, which facilitates integrity risk evaluation of URAIM. Therefore, the easy-to-implement URAIM approach seamlessly transitions between DRAIM and RRAIM, and enables to maintain a low probability of hazardous misleading information throughout the approach.

Performance evaluations are carried out for the shipboard Type B and SSM monitors and for the airborne DRAIM and URAIM approaches. The snapshot position and floating (real-valued) cycle ambiguity estimation algorithm exploits pre-filtered geometry-free measurements (using wide-lane carrier minus narrow-lane code signals) as well as current-time double-differenced carrier measurements.

It is noteworthy that fixing algorithms, which exploit the integer nature of cycle ambiguities [1], are instrumental in achieving demanding accuracy standards required in shipboard landing applications. However, the integrity monitoring performance analysis of fixed solutions can be extremely challenging. Fixing procedures are beyond the scope of this paper, which focuses on the preliminary design and analysis of new monitors.

The paper is organized as follows. Section II describes the estimation algorithm and discusses the impact of orbit ephemeris faults on position estimates. The shipboard and airborne monitors are respectively derived in Sec. III and IV and evaluated in Sec. V and VI. Concluding remarks are given in Sec. VII.

II. IMPACT OF ORBIT EPHEMERIS FAULTS ON CARRIER PHASE DIFFERENTIAL GPS

A. Two-Step Carrier Phase Differential GPS Algorithm

The carrier phase differential GPS algorithm described below provides relative positioning between aircraft and ship, as well as float differential cycle ambiguity estimates. Reliable communication between aircraft and ship is established within a predefined service volume (i.e., within the broadcast radius), where differential GPS is enabled. Measurements, including code and carrier signals at L1 and L2 frequencies, are exploited both inside and outside the service volume using a two-step process.

The first step is referred to as ‘geometry-free pre-filtering’. For each visible satellite, a narrow-lane code measurement is constructed as a weighted sum of L1 and L2 code signals, as described in [6] [7]. In parallel, a wide-lane carrier measurement is computed as a weighted difference of dual-frequency carrier signals. Narrow-lane code is differenced from wide-lane carrier to eliminate errors due to the ionosphere, to the troposphere, to satellite clock and orbit ephemeris, and to receiver clock. The differencing also eliminates dependency on satellite geometry (hence the term ‘geometry-free’).

The resulting observable provides a biased and noisy estimate of wide-lane cycle ambiguities. The small, quasi-constant offset caused by inter-frequency and antenna biases will be eliminated in the double-differencing process

performed when the aircraft enters the service volume. In addition, to reduce the impact of noise due to multipath and receiver noise, a running average of the cycle ambiguity estimates can be computed prior to entering the service volume (hence the term ‘pre-filtering’).

The second step is a ‘snapshot’ weighted least-squares position and cycle ambiguity estimation process, which uses the information from the first step as prior knowledge on wide-lane cycle ambiguities. Wide-lane carrier measurements are double-differenced: first between aircraft and ship to eliminate most of the spatially correlated errors (including ionospheric, tropospheric and satellite-related errors), and then with respect to a master satellite to eliminate receiver clock offsets. For consistency, pre-filtered measurements are also double-differenced, which eliminates the remaining frequency-dependent biases. The resulting observables (superscripts 1 to n) are stacked in a geometry-free (GF) measurement vector:

$$\mathbf{z}_{GF} = \begin{bmatrix} {}^1z_{GF} & \cdots & {}^nz_{GF} \end{bmatrix}^T$$

The double-differenced wide-lane carrier measurement vector is given by:

$$\boldsymbol{\phi}_{WL} = \begin{bmatrix} {}^1\phi_{WL} & \cdots & {}^n\phi_{WL} \end{bmatrix}^T$$

The complete measurement equation is expressed as:

$$\begin{bmatrix} \mathbf{z}_{GF} \\ \boldsymbol{\phi}_{WL} \end{bmatrix} = \begin{bmatrix} \mathbf{0} & \mathbf{I} \\ \mathbf{G} & \mathbf{I} \end{bmatrix} \begin{bmatrix} \mathbf{x} \\ \mathbf{n} \end{bmatrix} + \begin{bmatrix} \mathbf{v}_{GF} \\ \mathbf{v}_{WL} \end{bmatrix} \quad (1)$$

where

- \mathbf{I} is the identity matrix of appropriate dimensions
- \mathbf{v}_{GF} is the double-differenced geometry-free pre-filtered measurement noise vector
- \mathbf{v}_{WL} is the double-differenced wide-lane carrier phase measurement noise vector
- \mathbf{x} is the air-ship relative position vector (in a local reference frame, e.g., East-North-Up)
- \mathbf{G} is the matrix of differenced line of sight vectors for each satellite pair (expressed in a local reference frame)
- \mathbf{n} is the double-differenced wide-lane cycle ambiguity vector

The measurement noise vector \mathbf{v}_{GF} is made of code and carrier phase receiver noise and of time-correlated error due to multipath, which is modeled as a first order Gauss Markov process (GMP). The wide-lane carrier measurement noise vector \mathbf{v}_{WL} includes carrier multipath and receiver noise as well as remaining tropospheric and ionospheric decorrelation errors, which decrease as the aircraft comes closer to the ship. Both measurement noise vectors are assumed zero-mean, normally distributed. We use the notation:

$$\mathbf{v}_{GF} \sim \mathbf{N}(\mathbf{0}, \mathbf{V}_{GF}) \quad \text{and} \quad \mathbf{v}_{WL} \sim \mathbf{N}(\mathbf{0}, \mathbf{V}_{WL}).$$

The covariance matrices \mathbf{V}_{GF} and \mathbf{V}_{WL} are derived in App. I.

The fault-free measurement equation (1) is expressed in a general form as:

$$\mathbf{z} = \mathbf{H}\mathbf{u} + \mathbf{v} \quad (2)$$

where $\mathbf{v} \sim \mathcal{N}(\mathbf{0}, \mathbf{V})$ and the covariance matrix \mathbf{V} is also described in App. I. Matrix \mathbf{V} takes into account the time-correlation due to multipath between \mathbf{z}_{GF} and \mathbf{z}_{WL} , and the correlation across satellite pairs due to the common tropospheric errors.

An orbit ephemeris fault is modeled as a deterministic vector \mathbf{f} .

$$\mathbf{f} = [\mathbf{0} \quad \mathbf{f}_{WL}]^T$$

where
$$\mathbf{f}_{WL} = [{}^1f_{WL} \quad \dots \quad {}^nf_{WL}]^T. \quad (3)$$

It is worth noticing that faults do not affect the pre-filtering process because they are eliminated when differencing narrow-lane code from wide-lane carrier. Also, in this work, we assume that no more than one measurement is simultaneously impacted by a fault, so that only one of the fault coefficients ${}^i f_{WL}$ is non-zero. In the presence of a fault, (2) becomes:

$$\mathbf{z} = \mathbf{H}\mathbf{u} + \mathbf{v} + \mathbf{f} \quad (4)$$

We will use the notation $\delta\mathbf{z} = \mathbf{v} + \mathbf{f}$.

The weighted least squares state estimate error $\delta\mathbf{u}$ is defined as the difference between the state estimate $\hat{\mathbf{u}}$ and the true state vector \mathbf{u} ($\delta\mathbf{u} \equiv \hat{\mathbf{u}} - \mathbf{u}$). It is computed as:

$$\delta\mathbf{u} = \mathbf{S}\delta\mathbf{z}$$

where :
$$\mathbf{S} = (\mathbf{H}^T \mathbf{V}^{-1} \mathbf{H})^{-1} \mathbf{H}^T \mathbf{V}^{-1}$$

Let \mathbf{P} be the state estimate covariance matrix. \mathbf{P} is given by:

$$\mathbf{P} = (\mathbf{H}^T \mathbf{V}^{-1} \mathbf{H})^{-1}$$

In addition, performance analyses in Sec. V and VI focus on a single state δx , i.e., on the vertical position estimate. Let \mathbf{c}_x be a vector of zeros with a single one-coefficient that extracts the state of interest out of the full state vector:

$$\delta x = \mathbf{c}_x^T \delta\mathbf{u}$$

In the presence of a fault, we have:

$$\delta x \sim \mathcal{N}(\mathbf{c}_x^T \mathbf{S} \mathbf{f}, \sigma_x^2), \quad (5)$$

where we used the notation

$$\sigma_x^2 = \mathbf{c}_x^T \mathbf{P} \mathbf{c}_x$$

Before investigating the faulted case in more detail, the expression of σ_x^2 can be used to evaluate the fault-free integrity performance. The fault-free hypothesis is noted H0. The vertical protection level (or VPL) for H0 is defined as:

$$VPL_0 = \kappa_0 \sigma_x \quad (6)$$

where κ_0 is a probability multiplier corresponding to an integrity risk allocation of I_{H0} . An example integrity risk allocation tree is presented in Fig. 1 (the top-level allocation is similar to the one found in [8]).

The VPL in (6) is computed at the aircraft and compared to a specified vertical alert limit (VAL) to determine if the mission can be safely initiated. Under the fault-free hypothesis, an approach is deemed H0-available if throughout the mission:

$$VPL_0 < VAL \quad (7)$$

B. Description and Impact of Orbit Ephemeris Fault

Orbit ephemeris faults are rarely occurring deterministic errors. A failure rate of $10^{-4}/\text{hr}$ is specified in [9]. The mean time to detect such faults is guaranteed to be lower than 6 hr [10], and in this work is assumed to be 1 hr. The resulting assumed prior probability P_P of single satellite fault occurrence is 10^{-4} . The probability of multiple simultaneous faults is assumed to be zero. This assumption will be addressed in future work.

The fault vector \mathbf{f} in (4) represents an orbit ephemeris fault. It is caused by an unusually large difference between the actual spacecraft location and its computed position, which is estimated using the GPS ephemeris. Orbit ephemeris faults can be categorized in two fault types.

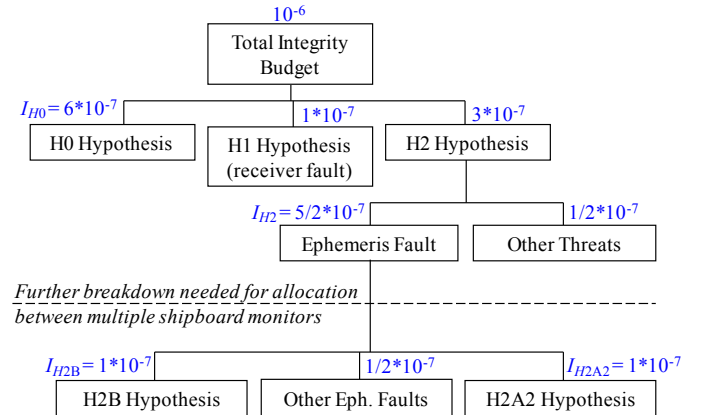


Figure 1. Example Integrity Risk Allocation Tree

- Type A faults designate events where satellite maneuvers are involved.
- Type B faults are blundered ephemerides occurring in the absence of maneuvers.

Type A faults can be caused by either intentional or unintentional thruster firing (causing orbit-tangential maneuvers) or by out-gassing (or fuel leakage) [10]. Satellite maneuvers are occasionally performed, for example to ensure that spacecraft remain in their designated slots. We distinguish the following kinds of type A faults:

- Type A1 faults correspond to orbit-tangential maneuvers where the ephemeris is blundered.
- Type A2 faults are also orbit-tangential maneuvers, but in this case, the pre-maneuver ephemeris is broadcast even though the maneuver has begun.
- Type A2' faults are caused by maneuvers in any direction while the pre-maneuver ephemeris is broadcast.

The GPS operational control segment (OCS) is in charge of performing spacecraft maneuvers and of monitoring satellite measurements at all times. If a maneuver is scheduled, or if a fault is detected, the OCS nominally sends a warning that the space vehicle (SV) signal should not be used (the satellite health flag is set to 'unhealthy'). In spite of the OCS monitoring, a Type A2 fault actually occurred on April 10 2007 [2]. It caused an error in satellite position that exceeded 700m before the satellite health flag was set to unhealthy. This type of rare-event faults can represent serious integrity threats for differential GPS-based navigation systems.

The impact on a differential measurement from satellite i of the ephemeris-based SV position error vector ${}^i\delta\mathbf{x}_E$ is expressed as:

$${}^i f = \frac{1}{r} \left((\mathbf{I} - {}^i\mathbf{e}^i\mathbf{e}^{iT}) {}^i\delta\mathbf{x}_E \right)^T \mathbf{d} \quad (8)$$

where

- ${}^i\mathbf{e}$ is the line of sight (LOS) vector between user and satellite i
- r is the nominal range to the satellite (about 20,000 km)
- \mathbf{d} is the baseline vector between aircraft and ship.

A complete derivation of (8) is given in [11]. An additional step is needed to obtain the fault impact on double-differenced measurements ${}^i f_{WL}$ in (3). This step is straightforward and is left aside for clarity of explanation.

Equation (8) shows that the fault impact on differential measurements depends on the relative directions of the fault and LOS vectors, and on the baseline vector \mathbf{d} between aircraft and ship antennas. The worst-case fault impact is found when the fault vector is perpendicular to the LOS vector, and aligned with the air-ship baseline vector. In this case, (8) becomes:

$${}^i f \leq \frac{{}^i\delta x_{E,\perp}}{r} d \quad (9)$$

where

${}^i\delta x_{E,\perp}$ is the fault component of ${}^i\delta\mathbf{x}_E$ perpendicular to the LOS vector; it is defined as a 2-norm (noted $\|\cdot\|$):

$${}^i\delta x_{E,\perp} \equiv \left\| (\mathbf{I} - {}^i\mathbf{e}^i\mathbf{e}^{iT}) {}^i\delta\mathbf{x}_E \right\|$$

the worst case fault direction is such that:

$${}^i\delta x_{E,\perp} = \left\| {}^i\delta\mathbf{x}_E \right\|.$$

d is the baseline distance between air and ship antennas.

Equation (9) first shows that nominal meter-level orbit ephemeris errors have a negligible impact (lower than 2.5 mm) on differential measurements over baseline distances as large as 50 km. Equation (9) also demonstrates that the 700 m SV positioning error experienced in the April 2010 incident could have caused a differential measurement fault of up to 17.5 cm over a short 5 km baseline. This fault magnitude can be a serious threat for shipboard landing applications. In response, both shipboard monitors and airborne RAIM-based algorithms are designed in Sec. III and IV.

III. SHIPBOARD MONITORS

A. Type B Monitor for Shipboard Landing of Aircraft

The type B monitor was designed and evaluated in [3] to detect faults affecting LAAS. In the absence SV maneuvers, it uses first-order hold projections of previously validated satellite orbits based on two days of stored ephemerides.

Reference [3] used the complete set of ephemerides for year 2002 to demonstrate that the Type B monitor achieved a 3000 m minimum detectable error (MDE, in terms of satellite position error), with a probability of no detection $P_{MDE,B}$ lower than $5*10^{-4}$.

In this work, the VPL for the Type B fault hypothesis (noted hypothesis H2B) is derived. The protection level is defined as a bound on the positioning error corresponding to an allocated integrity risk I_{H2B} (specified in Fig. 1).

$$P(\delta x > VPL_B) P_p \leq I_{H2B} \quad (10)$$

where

P_p is the prior probability of fault occurrence described in Sec. II

δx is the vertical position estimate error derived in (5).

The first term of the product in (10) is implicitly a conditional probability on the occurrence of H2B. Equation (10) is re-written considering two mutually exclusive, complementary hypotheses:

$$P(\delta x > VPL_B) = P(\delta x > VPL_B, \left\| {}^i\delta\mathbf{x}_E \right\| \leq MDE) + P(\delta x > VPL_B, \left\| {}^i\delta\mathbf{x}_E \right\| > MDE) \quad (11)$$

Each one of the right hand side terms can be bounded:

$$\begin{aligned} P(\delta x > VPL_B, \|\delta \mathbf{x}_E\| \leq MDE) \\ = P(\delta x > VPL_B \mid \|\delta \mathbf{x}_E\| \leq MDE) P(\|\delta \mathbf{x}_E\| \leq MDE) \\ \leq P(\delta x > VPL_B \mid \|\delta \mathbf{x}_E\| \leq MDE) \end{aligned}$$

$$\begin{aligned} P(\delta x > VPL_B, \|\delta \mathbf{x}_E\| > MDE) \\ = P(\delta x > VPL_B \mid \|\delta \mathbf{x}_E\| > MDE) P(\|\delta \mathbf{x}_E\| > MDE) \\ \leq P(\|\delta \mathbf{x}_E\| > MDE) \leq P_{MDE,B} \end{aligned}$$

Substituting the last two bounds back into (11) and the result into (10) yields:

$$P(\delta x > VPL_B \mid \|\delta \mathbf{x}_E\| \leq MDE) \leq I_{H2B}/P_p - P_{MDE,B} \quad (12)$$

The condition in the left-hand-side probability sets a bound on the magnitude of the satellite position error $\delta \mathbf{x}_E$, whose impact on the position estimate is expressed in (5) and (9). It follows that the VPL equation can be expressed as:

$$VPL_B = \kappa_B \sigma_X + \max_i |\mathbf{c}_X \mathbf{S}_{(:,i)}| \frac{MDE}{r} d \quad (13)$$

where

κ_B is a probability multiplier corresponding to the integrity risk allocation of $I_{H2B}/P_p - P_{MDE,B}$

$\mathbf{S}_{(:,i)}$ is the i^{th} column of matrix \mathbf{S} .

Similar to the fault-free case in (7), an approach is deemed available for the H2B hypothesis if:

$$VPL_B < VAL \quad (14)$$

The type B monitor is constraining because it requires a two day initialization period for ephemeris validation, which must be performed again each time an alarm is issued. More importantly, the type B monitor is only effective against orbit ephemeris faults that do not involve a maneuver. Therefore, other monitors are investigated.

B. Standalone Shipboard Monitor (SSM) Against Type A2 Faults

Unlike for the Type B monitor, current-time measurements must be used to detect if a maneuver has recently been performed. The LAAS Type A monitor uses measurements of range and range rates, but assumes a static reference antenna at a known location. Since shipboard antennas are continuously moving and are at unknown locations, the LAAS monitor cannot be used.

Instead, we develop a monitor that exploits the redundancy of satellite signals to evaluate the shipboard antenna's location while simultaneously monitoring SV measurements. This

standalone shipboard monitor (SSM) is based on a multiple-hypothesis range comparison method [12] [13].

One important observation can be made before describing the monitor. Equations (8) and (9) show that the fault impact on differential measurements (and hence on the estimate error in (5)) is maximized when the fault direction is perpendicular to the LOS. Unfortunately, faults perpendicular to the LOS are also mostly unobservable using standalone measurements. Therefore performance analyses in Sec. IV will show that the SSM is ineffective against Type A1 and Type A2' faults, which can have any direction. However, the SSM monitor turns out to be efficient against Type A2 faults, which involve orbit-tangential maneuvers.

A five-step description of the SSM is presented:

- we first define the test statistic
- we derive the detection threshold
- we establish a MDE in the standalone range domain
- this MDE is transferred into the differential measurement domain using a fault model
- and finally we compute a VPL equation for type A2 faults

For each satellite i , we compare the measured range ${}^i\rho_{meas}$ to satellite i with the computed range ${}^i\rho_{comp}$ obtained using the ephemeris. The measured range ${}^i\rho_{meas}$ is given by standalone (i.e., non-differential) ionospheric-error-free code phase measurements. The computed range ${}^i\rho_{comp}$ is the distance between the estimated SV position using the broadcast orbit ephemeris and the ship positioning sub-solution $\delta \mathbf{x}_{ship}^{(i)}$. The sub-solution $\delta \mathbf{x}_{ship}^{(i)}$ is based on all SVs except satellite i in order to avoid correlation of ${}^i\rho_{comp}$ with ${}^i\rho_{meas}$. The SSM test statistic ${}^i\Delta\rho$ is defined as:

$${}^i\Delta\rho = {}^i\rho_{meas} - {}^i\rho_{comp}$$

The test statistic ${}^i\Delta\rho$ is expressed as:

$${}^i\Delta\rho = {}^i v_{SVclock} + {}^i v_{tropo} + {}^i v_{RNM} - {}^i v_{OE,rad} - \mathbf{e}^T \delta \mathbf{x}_{ship}^{(i)} \quad (15)$$

where

- ${}^i v_{SVclock}$ is the nominal uncertainty due to satellite clock ephemeris
- ${}^i v_{tropo}$ is the standalone tropospheric error
- ${}^i v_{RNM}$ is the iono-free code receiver noise and multipath error
- ${}^i v_{OE,rad}$ is the nominal orbit ephemeris error projected onto the LOS vector. We will approximate this term by the radial satellite position error, whose contribution to the error along the LOS is much larger than the in-

track and cross-track components. The radial satellite position error has been evaluated in [14].

${}^i \mathbf{e}$ is the LOS vector to SV i

It is worth noticing that ${}^i \Delta \rho$ varies with satellite geometry, in particular because of the last term of the sum in (15).

Under fault-free conditions all terms in (15) are assumed normally distributed (with variances given in Sec. V) and are zero mean. Let ${}^i \sigma_{\Delta \rho}^2$ be the variance of ${}^i \Delta \rho$, which is computed as the sum of variances of all error terms in (15). A detection threshold ${}^i T$ is computed for each test statistic ${}^i \Delta \rho$ in order to reduce the probability of false alarms. The threshold ${}^i T$ is set in compliance with a continuity risk requirement P_C , which is equally allocated between each one of the n_{SV} test statistics. The threshold is computed as:

$${}^i T = Q^{-1}(P_C / n_{SV} / 2) {}^i \sigma_{\Delta \rho}$$

where $Q^{-1}(\cdot)$ is the inverse function of the tail probability of the standard normal distribution.

A fault on satellite i impacts the mean of ${}^i v_{OE,rad}$ which is equal to the mean noted ${}^i \mu$ of ${}^i \Delta \rho$. The MDE in the standalone ranging domain is noted $MDE_{\Delta \rho, i}$ and is defined as:

$$P({}^i \Delta \rho < {}^i T \mid {}^i \mu = MDE_{\Delta \rho, i}) \leq I_{MDE, A2} / P_P \quad (16)$$

where $I_{MDE, A2}$ is a predefined integrity risk allocation for the SSM monitor against Type A2 faults (we use $I_{MDE, A2} = 1/2 * 10^{-7}$). $MDE_{\Delta \rho, i}$ is obtained iteratively from (16).

In order to evaluate the impact of undetected faults on differential GPS position estimates, the MDE in the standalone range domain must be transferred into an MDE in the differential ranging domain. This is done numerically using a deterministic model of type A2 faults. Satellite maneuvers are simulated as instantaneous in-track burns, causing an instantaneous change in tangential velocity of Δv (realistic values of Δv range between 3 m/s and 5 m/s, but can reach up to 10 m/s [4]). Satellite maneuvers cause a drift over time of the true SV orbits as compared to the pre-maneuver ephemeris-based orbit.

In Fig. 2, the true SV orbits are represented in red for multiple start-times prior to current-time, and the computed orbit is the thick black line. For a range of realistic maneuver start times and Δv values, we can compute the current-time impact of the fault on the test statistic ${}^i \Delta \rho$. We can also evaluate the fault component perpendicular to the LOS ${}^i \delta x_{E,\perp}$, which directly impacts differential measurements in (9). It follows that the MDE in the differential measurement domain

is computed as:

$$MDE_{\delta x, i} = \max_{\substack{\text{model} \\ \text{parameters}}} \left({}^i \delta x_{E,\perp} \mid |{}^i \Delta \rho| < MDE_{\Delta \rho, i} \right)$$

Finally, given that $MDE_{\delta x, i}$ can be numerically evaluated, and using a derivation akin to (10) to (12), we establish a VPL equation for the SSM in the presence of Type A2 faults

$$VPL_{A2} = \kappa_{A2} \sigma_X + \max_i \left(\mathbf{c}_X \mathbf{S}_{(:,i)} \mid MDE_{\delta x, i} \right) \frac{d}{r} \quad (17)$$

where

κ_{A2} is a probability multiplier corresponding to the integrity risk allocation of $(I_{H2A2} - I_{MDE, A2}) / P_P$

I_{H2A2} is a predefined integrity allocation for Type A2 faults (given in Fig. 1)

When monitoring Type A2 faults using the SSM, an approach is deemed available if:

$$VPL_{A2} < VAL \quad (18)$$

The two shipboard monitors designed in this section aim at detecting Type A2 and Type B faults. However, these monitors are ineffective against type A1 and type A2' faults. In response, in Sec. IV, we explore the complementary properties of two airborne residual-based RAIM methods: differential RAIM and relative RAIM. The two concepts are exploited in the 'unified RAIM' approach, which provides detection capability against all types of faults in a single algorithm.

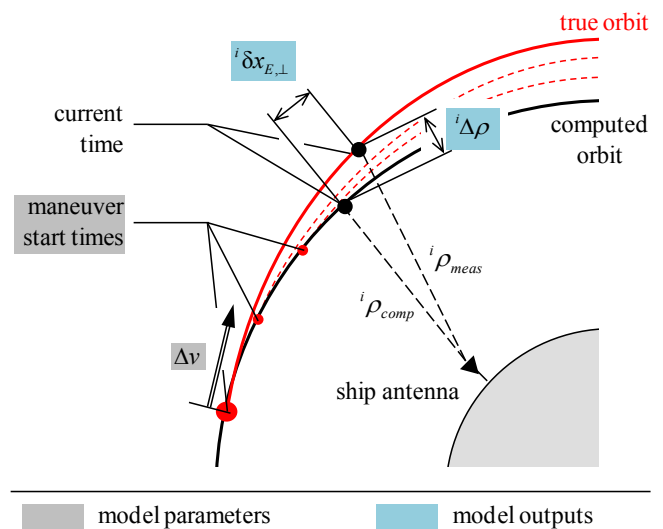


Figure 2. Type A2 Fault Model

IV. AIRBORNE MONITORS

A. Differential RAIM (DRAIM)

Differential RAIM is a least-squares residual-based RAIM method [15]. In DRAIM, differential carrier phase measurements are used to determine both the state estimates and the detection test statistic. The DRAIM residual vector is defined as:

$$\mathbf{r}_D \equiv \mathbf{z} - \mathbf{H}\mathbf{x} = \delta\mathbf{z} - \mathbf{H}\delta\mathbf{x} \quad (19)$$

The DRAIM test statistic is the norm of \mathbf{r}_D weighted by \mathbf{V}^{-1} [16]:

$$\|\mathbf{r}_D\|_{\mathbf{V}^{-1}}^2 = \mathbf{r}_D^T \mathbf{V}^{-1} \mathbf{r}_D \quad (20)$$

Let n be the total number of measurements (i.e., the dimension of \mathbf{z} in (4)), and let m be the number of unknown states (i.e., the dimension of \mathbf{x} in (4)). The weighted norm $\|\mathbf{r}_D\|_{\mathbf{V}^{-1}}^2$ is non-centrally chi-square distributed, with $(n-m)$ degrees of freedom and a non centrality parameter defined as:

$$\lambda_D^2 = \mathbf{f}^T \mathbf{V}^{-1} (\mathbf{I} - \mathbf{H}\mathbf{S}) \mathbf{f} \quad (21)$$

Under fault-free conditions, the detection threshold T_D is defined in compliance with the continuity risk requirement P_C to limit the probability of false alarms. The DRAIM integrity risk is then defined as a joint probability:

$$P(\delta x > VAL, \|\mathbf{r}_D\|_{\mathbf{V}^{-1}}^2 < T_D) \quad (22)$$

Because the estimate error and residual-based test statistic are stochastically independent [15], this joint probability can be written as a product of probabilities. It follows that the DRAIM integrity risk can then be computed for all single-SV faults and for all fault magnitudes.

Finally, in the presence of an orbit ephemeris fault (hypothesis H2), the DRAIM availability criterion is fulfilled if:

$$P(\delta x > VAL) P(\|\mathbf{r}_D\|_{\mathbf{V}^{-1}}^2 < T_D) < I_{H2} \quad (23)$$

where I_{H2} is a predefined integrity risk allocation (given in Fig. 1).

Considering (9) and (21), it is clear that as the aircraft approaches the ship's reference antenna, the fault's impact on the test statistic's non-centrality parameter decreases (the baseline distance d in (9) decrease). Performance analyses in Sec. VI will confirm that DRAIM is most effective in monitoring faults at the start of the aircraft approach, when the plane is far from the ship. But the DRAIM detection capability decreases as the aircraft approaches the crucial

touch-down point. As a complement to DRAIM, we investigate relative RAIM (RRAIM).

B. Relative RAIM (RRAIM)

The concept of RRAIM for shipboard landing applications was introduced in [5]. As illustrated in Fig. 3, a difference can be taken between measurements at the current-time epoch (carrier phase measurement vector Φ_{WL}) and at a past-time reference epoch (vector $\Phi_{WL,0}$), where the plane first entered the ship's broadcast radius. The RRAIM test statistic is derived from a vector Φ_{Δ^*} of time-differenced measurements:

$$\Phi_{\Delta^*} \equiv \Phi_{WL,0} - \Phi_{WL} \quad (24)$$

$$\Phi_{\Delta^*} = \mathbf{G}_0 \mathbf{x}_0 - \mathbf{G}\mathbf{x} + \mathbf{v}_{\Delta^*} \quad (25)$$

where

- \mathbf{G}_0 is the geometry matrix (matrix of LOS vectors) at the reference epoch
- \mathbf{x}_0 is the aircraft location at the reference epoch
- \mathbf{v}_{Δ^*} is the time-differenced carrier phase measurement noise vector defined as $\mathbf{v}_{\Delta^*} = \mathbf{v}_{WL,0} - \mathbf{v}_{WL}$

It is noteworthy that the vector of cycle ambiguities \mathbf{n} in (1) cancels out in (25), which signifies that RRAIM detection does not require cycle ambiguity resolution.

The time-difference between reference epoch and current-time epoch creates a synthetic baseline, which increases as the aircraft approaches the ship. As a result, the fault impact on the test statistic is small at the start of the approach, but increases as the aircraft comes closer to touch-down (because d in (9) is replaced by the synthetic baseline, which increases as the airplane approaches the ship). RRAIM aims at increasing fault-detection capability at the crucial touch-down point.

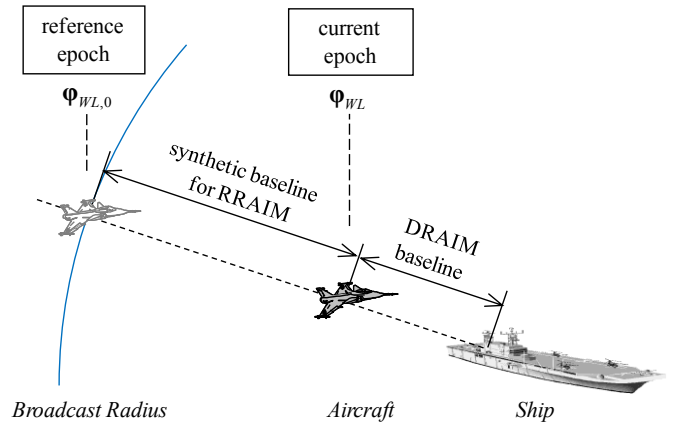


Figure 3. Overview of the RRAIM Concept

One major challenge in RRAIM is the computation of the integrity risk. The integrity risk is defined in (22) as a joint probability. For DRAIM, the random parts of the state estimates and of the test statistic were independent, so that the integrity risk could be computed as a product of probabilities in (23). In contrast, the RRAIM residual is shown in App. II to be correlated with state estimates. The correlation stems from the fact that, in RRAIM, different measurement equations are used for estimation (1) and for detection (25).

In App. II, we determine the component of the RRAIM residual that is independent of the estimate error. Unfortunately, the theoretical formula of this independent component can only be expressed in terms of measurement errors, and in practice, it cannot be computed as a function of the actual measurements. To circumvent this problem, the RRAIM concept is exploited using a unified RAIM approach.

C. Unified RAIM (URAIM)

The DRAIM and RRAIM concepts are unified using a single measurement equation that includes carrier phase signals both at the current-time epoch as in (1) and at the past-time reference epoch (also used in (25)). The URAIM measurement equation is expressed as:

$$\begin{bmatrix} \mathbf{z}_{GF} \\ \boldsymbol{\phi}_{WL} \\ \boldsymbol{\phi}_{WL,0} \end{bmatrix} = \begin{bmatrix} \mathbf{0} & \mathbf{I} & \mathbf{0} \\ \mathbf{G} & \mathbf{I} & \mathbf{0} \\ \mathbf{0} & \mathbf{I} & \mathbf{G}_0 \end{bmatrix} \begin{bmatrix} \mathbf{x} \\ \mathbf{n} \\ \mathbf{x}_0 \end{bmatrix} + \begin{bmatrix} \mathbf{v}_{GF} \\ \mathbf{v}_{WL} \\ \mathbf{v}_{WL,0} \end{bmatrix} + \begin{bmatrix} \mathbf{0} \\ \mathbf{f}_{WL} \\ \mathbf{f}_{WL,0} \end{bmatrix} \quad (26)$$

where $\mathbf{f}_{WL,0}$ is the impact of the fault on double-differenced wide-lane carrier phase measurements at the reference epoch. Equation (26) can be re-written as

$$\mathbf{z}_U = \mathbf{H}_U \mathbf{u}_U + \mathbf{v}_U + \mathbf{f}_U \quad (27)$$

The measurement noise vector is such that:

$$\mathbf{v}_U \sim \mathcal{N}(\mathbf{0}, \mathbf{V}_U)$$

The covariance matrix \mathbf{V}_U is computed as in App. I and takes into account the time-correlation between $\boldsymbol{\phi}_{WL}$ and $\boldsymbol{\phi}_{WL,0}$ due to multipath using a first order GMP.

State estimation in (1) to (5) is updated using (27). The resulting vertical position estimate is noted δx_U . Measurement equation (27) is not only used for estimation, but also for residual generation. URAIM is actually a direct application of residual-based RAIM. The resulting residual vector \mathbf{r}_U and its weighted norm are defined in the same way as \mathbf{r}_D in (19) and (20). $\|\mathbf{r}_U\|_{\mathbf{V}_U^{-1}}^2$ follows a non-central chi-square distribution, with $n_U - m_U$ degrees of freedom (where n_U and m_U respectively are the total numbers of measurements and of states in (26)) and a non-centrality parameter λ_U^2 defined as in (21).

It follows that the integrity risk can be directly computed because the estimate error and the residual-based test static are stochastically independent [15]. The availability criterion is expressed in terms of δx_U , $\|\mathbf{r}_U\|_{\mathbf{V}_U^{-1}}^2$, and of a test statistic T_U computed similarly to T_D for the URAIM test statistic. The criterion is expressed as:

$$P(\delta x_U > VAL) P\left(\|\mathbf{r}_U\|_{\mathbf{V}_U^{-1}}^2 < T_U\right) < I_{H2} \quad (28)$$

In addition, the algorithm seamlessly transitions between DRAIM and RRAIM. The integrity risk analysis in Sec. VI will show that the easy-to-implement URAIM approach efficiently exploits the complementary properties of DRAIM and RRAIM against all types of orbit ephemeris faults.

V. INTEGRITY ANALYSIS OF SHIPBOARD MONITORS

A. Framework for the Analysis and Fault-Free Performance

Performance analyses are structured around the example mission of a simplified straight-in trajectory, where the aircraft approaches the ship at constant 150 knot velocity, with a constant 3 deg glideslope angle. Approaches start 15 nmi away from the ship. Prior to that, the aircraft may be maneuvering with a high banking angle causing satellites to be masked by the fuselage. Therefore, the aircraft pre-filtering process is launched at the approach start-time. The pre-filtering period increases from 0 to 6 min as the aircraft comes closer to touch-down. The ship pre-filtering process starts when the satellite rises, assuming that shipboard receivers are continuously operating.

A nominal 24 GPS satellite constellation is considered [10]. Geometries are simulated at regular 2 min intervals over a 24 hour period, which amounts to 720 sample geometries per location. A 10 deg elevation mask is implemented. It causes occurrences of geometries where fewer than five satellites are visible. In these cases, redundancy based monitors (SSM and RAIM) are ineffective.

Poor geometries also cause fault-free unavailability hits, as shown in Fig. 4, at an example location in the Pacific Ocean (30 deg North latitude, -150 deg East longitude). Fig. 4 illustrates how availability is established for each approach, and over 24 hours. The 720 thin colored curves represent VPL_0 for air-ship separation distances of 10 nmi to 0 nmi. The ratio of the number curves that are fully below the example VAL profile (thick black line) over 720 is the fault-free availability performance. In this case, H0-availability is 95.7%, which is one of the lowest values found for the grid of location represented below in the next figures. Notice that the example VAL requirement tightens as the aircraft approach touch-down. At the same time, estimation performance improves because pre-filtering period increases. Still, unavailability hits occur during the last 0.5 nmi.

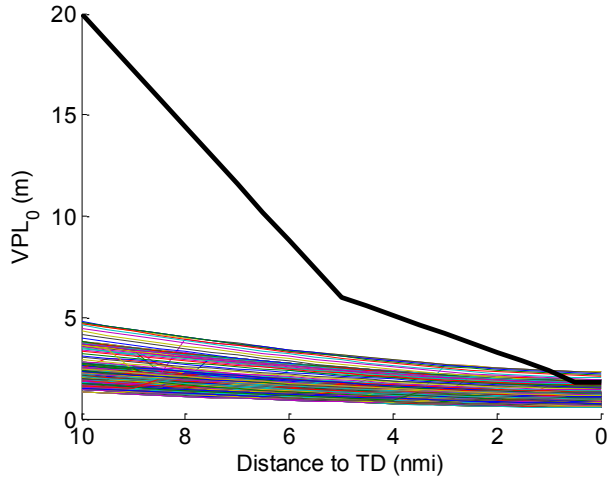


Figure 4. Fault-Free VPL over Distance to Touch Down

In the remainder of this paper, overall performance results are presented in terms of combined availability of fault-free integrity, and of integrity under faulted conditions, for each monitor that is being investigated. Throughout the paper, we have derived a four availability criteria (one per monitor) under faulted conditions, expressed in (14), (18), (23) and (28). The combined availability for each monitor is satisfied only if both the H0 criterion and the monitor's criterion are satisfied. Therefore, H0-availability limits combined availability. However, we have observed that in the overwhelming majority of cases, geometries that are H0-unavailable are also unavailable according to each monitor's criterion.

H0-availability was also evaluated for a 10 deg by 10 deg grid of 44 locations over the northern Pacific Ocean. Fig. 5 presents the H0-availability map. Availability is color-coded from white, representing 100%, to black, corresponding to 90% or lower. Contours of constant availability are displayed as well. The map shows that H0-availability varies between 95% and 100%.

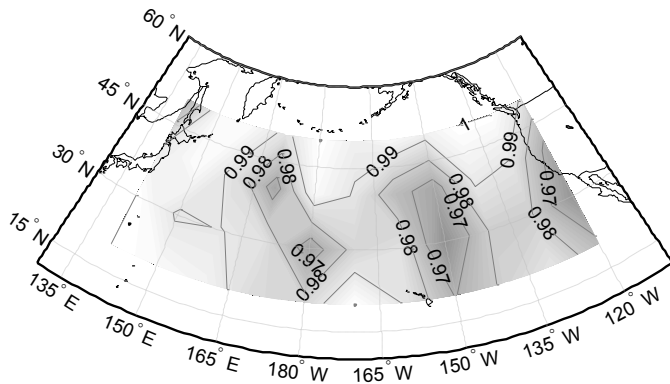


Figure 5. Availability Map for the Fault-Free Availability Criterion

B. Type B Monitor Performance Evaluation

Combined availability for the Type B monitor is represented in Fig. 6 for the grid of 44 locations. Availability performance ranges between 95% and 99%, and is only slightly lower than H0-availability. This shows that the Type B monitor efficiently detects Type B faults. However, the type B monitor can be constraining because of its required two-day initialization period. In addition, it is ineffective in case of SV maneuvers, which is why we quantify the SSM performance.

C. SSM Performance Evaluation Against Type A2 Faults

The SSM was designed in Sec. III to detect Type A2 faults, which are modeled in Fig. 2. The monitor's test statistic ${}^i\Delta\rho$ is evaluated using (15). The standard deviations of error parameters affecting ${}^i\Delta\rho$ are listed and referenced in Table I. Using these values, the monitor's MDE in the standalone range domain ($MDE_{\Delta\rho,i}$) is computed for each geometry and transferred in the differential measurement domain. $MDE_{\Delta\rho,i}$ values were computed for numerous geometries. We determined that 30 m was an optimistic $MDE_{\Delta\rho,i}$ -value.

Combined availability of the SSM against Type A2 faults is evaluated in Fig. 7. We considered the following values for the Type A2 fault model parameters :

- maneuver start times varying between 0 and 1 hour prior to current time
- Δv ranging between 2 m/s and 5 m/s

Despite the fact that we used a realistic but not necessarily conservative range of values for these parameters, availability performance remains below 95% at most locations. Availability drop below 50% if we increase maneuver start times to two hours prior to current time.

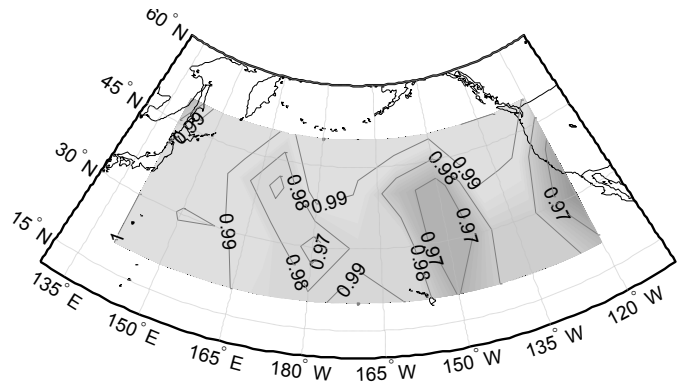


Figure 6. Combined Availability Map for the Type B Monitor Against Type B Faults

TABLE I. SSM MONITOR PARAMETERS

Error Source	Standard Deviation	Reference
Satellite clock	$\sigma_{SVclock} = 1.7$ m	[14]
Satellite ephemeris (orbit-radial)	$\sigma_{OE,rad} = 1.5$ m	[14] [17]
Troposphere (zenith error)	$\sigma_{tropo} = 0.12$ m	[18]
Iono-free code receiver noise and multipath	$\sigma_{RNM} = 1.05$ m	App. I
These values are also used to compute the uncertainty in the ship positioning sub-solution $\delta x_{ship}^{(i)}$ in (15)		

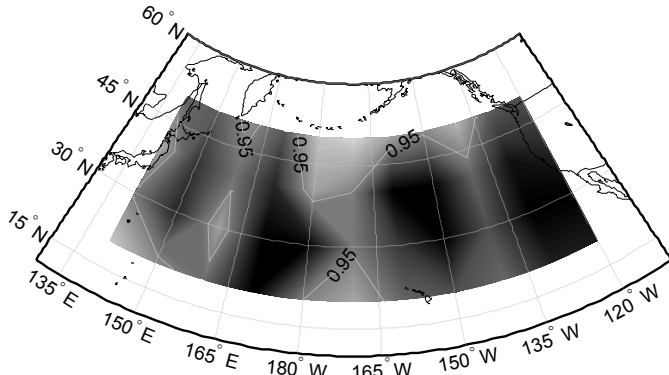


Figure 7. Combined Availability Map for the SSM Against Type A2 Faults

Type A2 faults are further investigated in Fig. 8 using the fault model of Fig. 2 at the near-worst example location used in Fig. 4, and for the model parameter values mentioned above. The curves capture Type A2 fault signatures for varying maneuver start times. Colored curves represent the fault impact on the standalone range error, i.e., on the SSM test statistic ${}^i\Delta\rho$, versus the magnitude of the fault component perpendicular to the LOS, noted ${}^i\delta x_{E,\perp}$ in (9). Considering the optimistic 30 m $MDE_{\Delta\rho,i}$, all colored curves correspond to potentially undetected faults. We only represent faults causing ${}^i\Delta\rho$ to be negative before becoming positive. This type of faults are the most hazardous because they remain undetected over the longest durations. They occur on rising satellites, and become hazardous for Δv values larger than 3m/s. In these cases, the orbit-tangential maneuver pushes the spacecraft towards the user antenna at a higher rate than the true orbit drifts away from the pre-maneuver orbit.

We distinguish two families of curves. The ones that start at the origin correspond to maneuvers that were initiated while the SV was in view. For all the other curves, which are inside the red trapezoid, the maneuver started out of view (thus, the zero crossing is not visible). One remarkable feature of this second family of curves is that, unlike the first family, the fault start time is known: indeed, although the maneuver start time is unknown, we know that the fault starts affecting measurements at signal acquisition. If the time to detect these faults is short enough, these threats can be eliminated by simply imposing a waiting period.

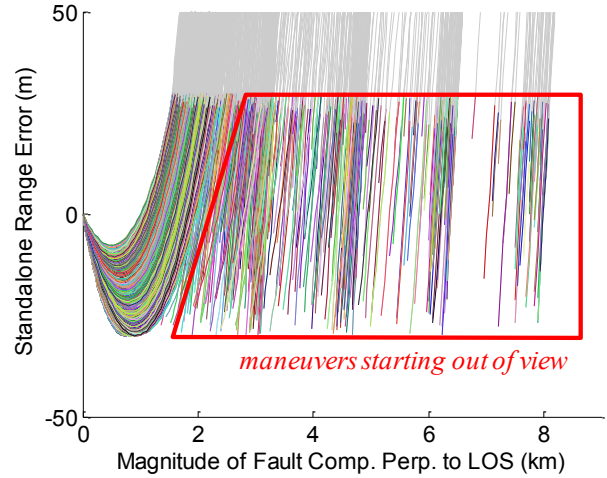


Figure 8. Type A2 Fault Signatures

A histogram of time-to-detect is presented in Fig. 9 for all curves presented in Fig. 8. The bins' multi-modal aspect on the right hand side comes from the fact that we simulated discrete values of Δv . Faults corresponding to maneuvers starting out of view (inside the trapezoid in Fig. 8) are identified inside a red box. Their time to detect is within 5 min. Therefore, imposing a 5 min waiting period after signal acquisition at the ship gets rid of these faults. Again, faults corresponding to maneuvers starting while in view cannot be as easily eliminated, but they have a lower impact ${}^i\delta x_{E,\perp}$ on differential measurements, as shown on the x-axis in Fig. 8.

Finally, the SSM combined availability performance is re-evaluated in Fig. 10, assuming that a 5 min waiting period is implemented at the ship after signal acquisition. The comparison between Fig. 7 and Fig. 10 shows the benefit of this modification.

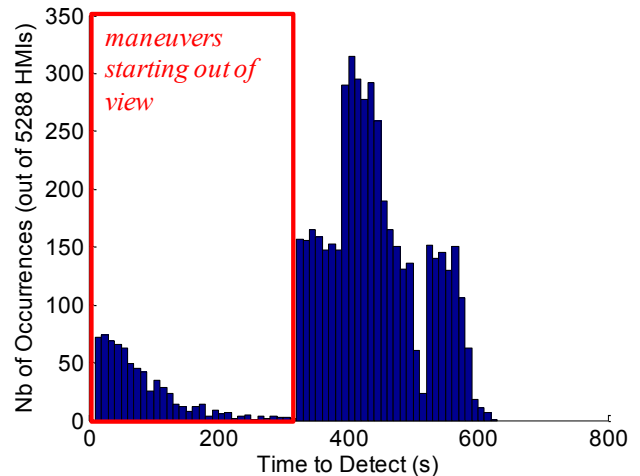


Figure 9. Histogram of SSM's Time to Detect Type A2 Faults

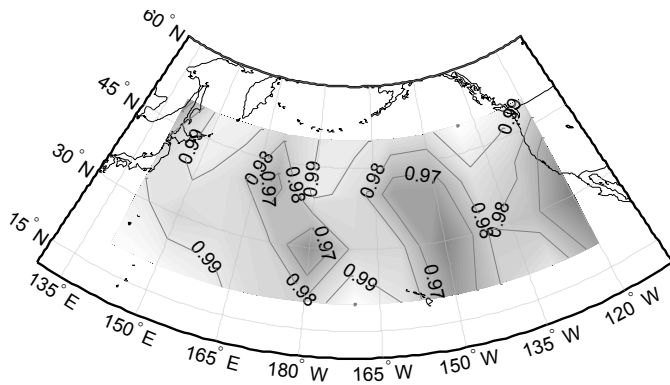


Figure 10. Combined Availability Map for the SSM Against Type A2 Faults, Assuming a 5 min Waiting Period

D. SSM Performance Evaluation Against Type A1 and A2' Faults

Fig. 10 shows that the SSM can be efficient in detecting Type A2 faults. However, it is ineffective against Type A1 and Type A2' faults, which can have any direction. For example, faults perpendicular to the LOS directly impact differential measurements (as explained in (9)) but are mostly unobservable using standalone measurements. To emphasize this point, rather than showing poor availability results, we simply evaluate the impact of faults perpendicular to the LOS on ${}^i\Delta\rho$ versus ${}^i\delta x_{E,\perp}$. The result is presented in Fig. 11, for faults simulated during 24 hours at 2 min intervals. It shows that the fault impact on ${}^i\Delta\rho$ remains far below an optimistic 30 m $MDE_{\Delta\rho,i}$ (i.e., these faults would not be detected) while ${}^i\delta x_{E,\perp}$ reaches 30 km, which is clearly hazardous. For comparison, the Type B monitor analysis showed that unavailability hits started occurring while the fault magnitude was limited to 3km. Also, we determined that a 10km ${}^i\delta x_{E,\perp}$ causes the availability to drop to 30% at the example near-worst location mentioned in Sec. V-A.

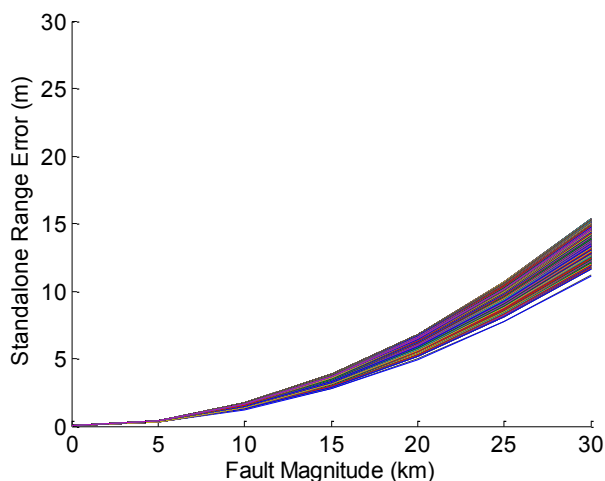


Figure 11. Impact of Faults Normal to the Line-of-Sight on the SSM Test Statistic, and on Differential Measurements

VI. INTEGRITY ANALYSIS OF AIRBORNE MONITORS

Section V has shown that shipboard monitors perform well, but only against two targeted fault types. In contrast, the integrity risk of RAIM-based algorithms is evaluated for the worst case fault magnitude, assuming the worst case impact on differential measurements. This section demonstrates that a unified airborne RAIM algorithm can be used instead of multiple shipboard monitors, and that URAIM can be efficient against all fault types.

A. DRAIM Performance Evaluation

To illustrate DRAIM, Fig. 12 presents point-wise combined availability performance, at the example location used in Sec. V-A. In Fig. 12, each point of the thin black line represents the DRAIM availability performance at a fixed distance from touch-down. These numbers are not necessarily representative of the overall performance (overall availability is given in the legend). However, point-wise availability shows where unavailability hits occur during approaches. As expected, DRAIM performs well for large air-ship separation distances. But DRAIM availability drops when the aircraft approaches the ship, both because VAL requirements are more stringent, and because DRAIM fault-detection capability decreases. At the touch-down point, the curve goes back to the fault-free level because the fault magnitude is zero ($d=0$ in (9)). The URAIM approach deals with DRAIM's drop in availability using the RRAIM concept.

B. URAIM Performance Analysis

The URAIM method unifies DRAIM and RRAIM and exploits the complementary properties of both algorithms. This is illustrated in Fig. 12 where the thick red curve maintains a high level of availability throughout the approach, while DRAIM availability drops dramatically in the last 5 nmi before touch-down.

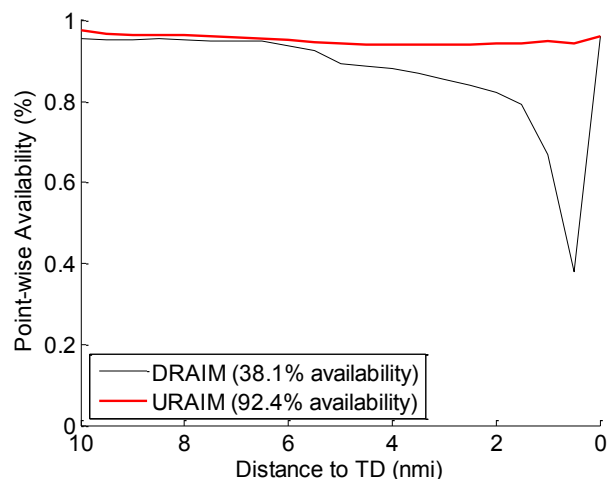


Figure 12. Point Wise Availability of DRAIM and RAIM at a Single Location

To further investigate URAIM performance, the map in Fig. 13 displays combined availability of fault-free integrity and of integrity using URAIM in the presence worst-case orbit ephemeris faults. Availability results are slightly lower than H0-availability in Fig. 5, which indicates that most but not all hazardous faults are detected using URAIM. Still, combined availability is higher than 94% at all locations.

The results presented in Sec. V and VI only took into account integrity risk requirements. However, navigation systems for shipboard landing of aircraft must also satisfy demanding accuracy standards. These can be fulfilled using advanced fixing processes [1], which exploit the integer nature of cycle ambiguities. Cycle ambiguity resolution processes are likely to improve fault-free availability. With regard to URAIM availability, two conflicting mechanisms can interfere. On the one hand, the estimation error of the fixed solution decreases as compared to the float implementation presented here. On the other hand, the probability of incorrect fix must be correctly accounted for in the integrity risk evaluation. Therefore, the next step of this monitor design process is to evaluate the navigation system accuracy and integrity performance for the fixed implementation.

VII. CONCLUSION

In this work, we devise a standalone shipboard monitor (SSM) and a unified RAIM (URAIM) algorithm. These new methods aim at detecting orbit ephemeris faults impacting carrier phase differential GPS signals used in a precision navigation application of shipboard landing of aircraft.

The SSM is based on a multiple-hypothesis range comparison approach. It uses non-differential, dual-frequency code measurements at the ship to detect faults on carrier phase differential measurements. Performance evaluations show that the SSM is efficient against Type A2 faults, provided that a 5 min waiting period is imposed after signal acquisition at the ship receiver. In addition, the LAAS Type B monitor performance is quantified. For this shipboard landing application, the Type B monitor demonstrates high detection capability against Type B faults. However, neither of the shipboard monitors are effective against Type A1 and Type A2' faults.

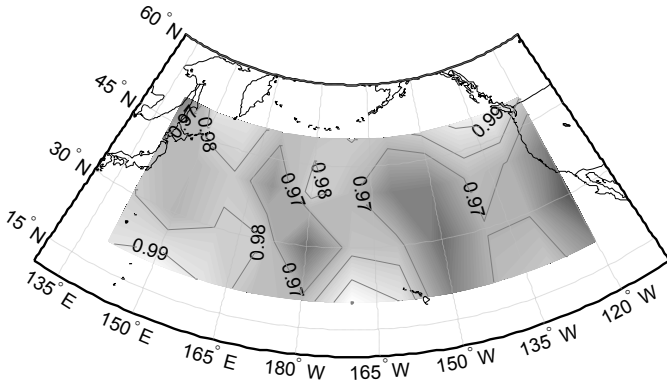


Figure 13. Combined Availability Map of URAIM Against all Fault Types

In response, a residual-based unified RAIM approach is investigated. URAIM exploits complementary properties of differential RAIM and of relative RAIM in order to maintain a low integrity risk throughout the airplane's approach. The airborne URAIM method is a single, easy-to-implement algorithm. It can be used in place of multiple shipboard monitors to detect all types of orbit ephemeris faults.

Overall performance was computed for a grid of 44 locations. For URAIM, availability ranges between 94% and 99%. These results are established for a float cycle ambiguity estimation process. Additional information of the cycle ambiguities' integer nature will be exploited in future work using a fixing algorithm. A cycle ambiguity fixing process will reduce positioning errors, and in turn, is expected to improve the integrity monitoring performance.

APPENDIX I. MEASUREMENT ERROR COVARIANCE MATRIX

The measurement error covariance matrix \mathbf{V} of \mathbf{v} in (2) and (4) can be expressed as:

$$\mathbf{V} = \begin{bmatrix} \mathbf{V}_{GF} & \mathbf{V}_C \\ \mathbf{V}_C & \mathbf{V}_{WL} \end{bmatrix}$$

The matrix \mathbf{V}_{GF} is fully described in Chapter 2 of [1].

In this work, \mathbf{V}_{WL} is defined as:

$$\mathbf{V}_{WL} = \mathbf{T}_{DD} (\mathbf{V}_{RNM,SD} + \mathbf{V}_{I,SD} + \mathbf{V}_{T,SD}) \mathbf{T}_{DD}^T$$

where

\mathbf{T}_{DD} is a $(n_{SV} - 1) \times n_{SV}$ transformation matrix that differences the measurements with the master SV signal (n_{SV} is the number of visible SVs); assuming that the first satellite is the master SV, we have:

$$\mathbf{T}_{DD} = \begin{bmatrix} -1 & 1 & 0 & \dots & 0 \\ -1 & 0 & 1 & \ddots & \vdots \\ \vdots & & \ddots & \ddots & 0 \\ -1 & 0 & \dots & 0 & 1 \end{bmatrix}$$

$\mathbf{V}_{RNM,SD}$ is the single-difference (air-ship) widelane carrier phase receiver noise and multipath error covariance matrix, defined as:

$$\mathbf{V}_{RNM,SD} = \mathbf{I} (2\sigma_{\phi,WL}^2)$$

$\sigma_{\phi,WL}^2$ is defined in Chapter 2 of [1] as a function of the raw carrier phase receiver noise and multipath standard deviation σ_{ϕ} (assuming the same σ_{ϕ} -value for L1 and L2)

$\mathbf{V}_{I,SD}$ is the residual ionospheric error covariance matrix (after air-ship single-difference). $\mathbf{V}_{I,SD}$ is diagonal,

with diagonal elements for a satellite i :

$$\left(\mathbf{V}_{I,SD}\right)_{i,i} = \left(d c({}^i\theta)\right)^2 \sigma_{VIG}^2$$

where d is defined in (9), σ_{VIG}^2 is the variance of the vertical ionospheric gradient, and $c({}^i\theta)$ is an obliquity factor defined in [19] as a function of the satellite elevation angle ${}^i\theta$.

$\mathbf{V}_{T,SD}$ is the residual tropospheric error. It is expressed as:

$$\mathbf{V}_{T,SD} = \mathbf{c}_{tropo} \mathbf{c}_{tropo}^T \sigma_{\Delta n}^2$$

where $\sigma_{\Delta n}^2$ is the variance of the tropospheric refractivity index, as defined in [19]. \mathbf{c}_{tropo} is derived from a vector of tropospheric obliquity coefficients (varying with ${}^i\theta$) multiplied by a function of the airship height difference (see [19] for details).

In addition, we derive an expression of the correlation caused by time-correlated multipath errors affecting wide-lane carrier signals in both \mathbf{z}_{GF} and $\boldsymbol{\phi}_{WL}$. The matrix \mathbf{V}_C can be written as:

$$\mathbf{V}_C = \mathbf{T}_{DD} \mathbf{V}_{C,SD} \mathbf{T}_{DD}^T$$

Matrix $\mathbf{V}_{C,SD}$ is diagonal, with diagonal elements for each satellite i :

$$\left(\mathbf{V}_{C,SD}\right)_{i,i} = \lambda_{WL} \sigma_{\phi,WL}^2 \left(\frac{\tau_M}{\tau_i} \left(1 - e^{-\tau_i/\tau_M} \right) \right)$$

where

- λ_{WL} is the wavelength of the wide-lane frequency (defined in [1])
- τ_M is the time constant of the first order GMP used to model multipath
- τ_i is the pre-filtering period for SV i .

Parameter values used in performance evaluations are summarized in Table II.

TABLE II. SUMMARY OF ERROR PARAMETER VALUES

Error Source	Parameter	Value
Raw carrier receiver noise and multipath	σ_ϕ	0.7 cm
Raw code receiver noise and multipath	σ_ϕ	35 cm
Vertical ionospheric gradient	σ_{VIG}^2	4 mm/km
Tropospheric refractivity index	$\sigma_{\Delta n}^2$	10
Multipath correlation time constant	τ_M	60 s

APPENDIX II. ANALYSIS OF THE RRAIM TEST STATISTIC

In this appendix, we prove that the RRAIM residual is not stochastically independent of the estimate error. In addition, we derive an analytical formula of the component of the residual that is independent of the estimate error.

The derivation starts with the measurement equation (25), to which a null-quantity is added:

$$\boldsymbol{\phi}_{\Delta^*} = \mathbf{G}_0 \mathbf{x}_0 + (-\mathbf{G} \mathbf{x}_0 + \mathbf{G} \mathbf{x}_\Delta) - \mathbf{G} \mathbf{x} + \delta \boldsymbol{\phi}_{\Delta^*}$$

$$\boldsymbol{\phi}_{\Delta^*} = \mathbf{G}_\Delta \mathbf{x}_0 + \mathbf{G} \mathbf{x}_\Delta + \delta \boldsymbol{\phi}_{\Delta^*}$$

where $\mathbf{G}_\Delta = \mathbf{G}_0 - \mathbf{G}$ and $\mathbf{x}_\Delta = \mathbf{x}_0 - \mathbf{x}$.

and $\delta \mathbf{z}_{\Delta^*} = \mathbf{v}_{\Delta^*} + \mathbf{f}_{\Delta^*}$.

We used the notation \mathbf{f}_{Δ^*} to designate the fault impact on $\boldsymbol{\phi}_{\Delta^*}$. The magnitude of \mathbf{f}_{Δ^*} increases as the aircraft approaches the ship.

We can use the aircraft position estimate $\hat{\mathbf{x}}_0$ at the reference epoch to rewrite the measurement equation as:

$$\boldsymbol{\phi}_{\Delta^*} - \mathbf{G}_\Delta \hat{\mathbf{x}}_0 = \mathbf{G} \mathbf{x}_\Delta + (\delta \boldsymbol{\phi}_{\Delta^*} - \mathbf{G}_\Delta \delta \mathbf{x}_0)$$

Therefore, the measurement equation used to establish the RRAIM test statistic takes the form:

$$\boldsymbol{\phi}_\Delta = \mathbf{G} \mathbf{x}_\Delta + \delta \boldsymbol{\phi}_\Delta$$

From the RRAIM measurement equation, we can define a weighted pseudo-inverse matrix \mathbf{S}_Δ in the same manner as we defined \mathbf{S} at the current-time epoch. It follows that the RRAIM residual is defined as:

$$\mathbf{r}_\Delta \equiv \boldsymbol{\phi}_\Delta - \mathbf{G} \mathbf{x}_\Delta = (\mathbf{I} - \mathbf{G} \mathbf{S}_\Delta) \delta \boldsymbol{\phi}_\Delta$$

In order to discuss independence of estimate error and test statistic, we must express them both as a function of the same random noise vectors. In this perspective, we define a matrix \mathbf{E}_Z that extracts $\boldsymbol{\phi}_{WL}$ from \mathbf{z} in (1)-(2):

$$\mathbf{E}_Z = \begin{bmatrix} \mathbf{0} & \mathbf{I}_n \end{bmatrix}$$

where the subscript of \mathbf{I} indicates the dimension of the identity matrix ($n = n_{SV}-1$).

The RRAIM residual becomes:

$$\mathbf{r}_\Delta = (\mathbf{I} - \mathbf{G} \mathbf{S}_\Delta) (\delta \boldsymbol{\phi}_{\Delta^*} - \mathbf{G}_\Delta \delta \mathbf{x}_0)$$

$$\mathbf{r}_\Delta = (\mathbf{I} - \mathbf{G} \mathbf{S}_\Delta) (\mathbf{E}_Z (\delta \mathbf{z}_0 - \delta \mathbf{z}) - \mathbf{G}_\Delta \delta \mathbf{x}_0)$$

The current time estimate error in (4)-(5) is expressed as a

function of $\delta \mathbf{z}$. Assuming that measurements at current time and at the reference epoch are not correlated (which is reasonable if RRAIM is used close to the ship), the random parts of $\delta \mathbf{z}$ are independent of $\delta \mathbf{z}_0$ and of $\delta \mathbf{x}_0$. Therefore, the part of \mathbf{r}_Δ that might not be dependent of the estimate error is:

$$(\mathbf{I} - \mathbf{G}\mathbf{S}_\Delta)\mathbf{E}_z\delta \mathbf{z}$$

Reference [20] proves that the random parts of the state estimate $\mathbf{S}\delta \mathbf{z}$ and of the residual \mathbf{r} are derived from orthogonal components of the measurement error. We can identify these components by going back to estimate error definition ($\delta \mathbf{u} \equiv \hat{\mathbf{u}} - \mathbf{u}$), and substituting \mathbf{u} into (4), which results in:

$$\delta \mathbf{z} = \mathbf{H}\delta \mathbf{u} + \mathbf{z} - \mathbf{H}\hat{\mathbf{u}}$$

$$\delta \mathbf{z} = \mathbf{H}\mathbf{S}\delta \mathbf{z} + \mathbf{r}$$

The first term of the sum $\mathbf{H}\mathbf{S}\delta \mathbf{z}$ is the component of the measurement error used for estimation. It follows that the component of the RRAIM residual that is not independent of the estimate error is:

$$\mathbf{r}_{NI} = -(\mathbf{I} - \mathbf{G}\mathbf{S}_\Delta)\mathbf{E}_z\mathbf{H}\mathbf{S}\delta \mathbf{z}$$

In general, \mathbf{r}_{NI} is not zero. It means that the RRAIM residual is not independent of the estimate error, which prevents direct evaluation of the integrity risk.

Still, we can identify the component \mathbf{r}_I of the residual that is independent of the estimate error:

$$\mathbf{r}_I = \mathbf{r}_\Delta - \mathbf{r}_{NI} = (\mathbf{I} - \mathbf{G}\mathbf{S}_\Delta)(\delta \boldsymbol{\varphi}_\Delta + \mathbf{E}_z\mathbf{H}\mathbf{S}\delta \mathbf{z})$$

We could use the weighted norm of \mathbf{r}_I as a test statistic (as in (20)), which would enable integrity risk evaluation. Unfortunately, \mathbf{r}_I is expressed in terms of the measurement error vectors $\delta \boldsymbol{\varphi}_\Delta$ and $\delta \mathbf{z}$ instead of measurements $\boldsymbol{\varphi}_\Delta$ and \mathbf{z} . \mathbf{r}_I cannot be computed in practice. In response, we use RRAIM in conjunction with DRAIM in the unified RAIM algorithm derived in Sec. IV-C.

REFERENCES

[1] S. Khanafseh and B. Pervan, "A New Approach for Calculating Position Domain Integrity Risk for Cycle Resolution in Carrier Phase Navigation Systems," *IEEE Transactions on Aerospace and Electronic Systems*, Vol. 46, No. 1, 2010, pp. 296-307.

[2] Federal Aviation Administration GPS Product Team, "Global Positioning System Standard Positioning Service Performance Analysis

Report" Report #58, June 31, 2007, available online at <http://www.nstb.tc.faa.gov/DisplayArchive.htm>

[3] B. Pervan, and L. Gratton, "Orbit Ephemeris Monitors for Local Area Differential GPS," *IEEE Transactions on Aerospace and Electronic Systems*, Vol. 41, No.2, 2005.

[4] H. Tang, S. Pullen, P. Enge, L. Gratton, B. Pervan, M. Brenner, J. Scheitlin, and P. Kline, "Ephemeris Type A Fault Analysis and Mitigation for LAAS," *Proc. IEEE/ION PLANS 2010*, Indian Wells, CA, 2010.

[5] M. Heo, B. Pervan, S. Pullen, J. Gautier, P. Enge, and D. Gebre-Eziabher, "Robust Airborne Navigation Algorithm for SRGPS," *Proc. of IEEE/ION PLANS*, Monterey, CA, 2004.

[6] M. Heo, "Robust Carrier Phase DGPS Navigation for Shipboard Landing of Aircraft," PhD Dissertation, Illinois Institute of Technology, Chicago, IL, 2004.

[7] S. Khanafseh, "GPS Navigation Algorithms for Autonomous Airborne Refueling of Unmanned Air Vehicles," PhD Dissertation, Illinois Institute of Technology, Chicago, IL, 2008.

[8] S. Wu, S. Peck, and R. Fries, "Geometry Extra-Redundant Almost Fixed Solutions: A High Integrity Approach for Carrier Phase Ambiguity Resolution for High Accuracy Relative Navigation," *Proc. of IEEE/ION PLANS 2008*, Monterey, CA, 2008, pp. 568-582.

[9] Federal Aviation Administration, "Category I Local Area Augmentation System Ground Facility," FAA-E-2937A, 2002.

[10] Assistant Secretary of Defense for Command, Control, Communications and Intelligence, "Global Positioning System Standard Positioning Service Performance Standard, 4th Edition," Washington, DC, 2008, available online at www.pnt.gov/public/docs/2008/spgps2008.pdf.

[11] F. C. Chan, "Detection of Global Positioning Satellite Orbit Errors Using Short-Baseline Carrier Phase Measurements," MS Thesis, Illinois Institute of Technology, Chicago, IL, 2001.

[12] Y. C. Lee, "Analysis of Range and Position Comparison Methods as a Means to Provide GPS Integrity in the User Receiver," *Proc. 42nd Annual Meeting of ION*, Seattle, WA, 1986, pp. 1-4.

[13] R. Brown, "A Baseline RAIM Scheme and a Note on the Equivalence of Three RAIM Methods," *NAVIGATION: Journal of the Institute of Navigation*, Vol. 39, No. 4, 1992, pp. 127-137.

[14] C. Cohenour, and F. van Graas, "GPS Orbit and Clock Error Distributions," *NAVIGATION: Journal of the Institute of Navigation*, Vol. 58, No. 1, 2011, pp. 17-28.

[15] M. Sturza, "Navigation System Integrity Monitoring Using Redundant Measurements," *NAVIGATION: Journal of the Institute of Navigation*, Vol. 35, No. 4, 1988, pp. 69-87.

[16] T. Walter, and P. Enge, "Weighted RAIM for Precision Approach," *Proc. ION GPS*, Palm Springs, CA, 1995.

[17] D. Warren, and J. Raquet, "Broadcast vs Precise GPS Ephemerides: A Historical Perspective," *Proc. ION NTM*, San Diego, CA, 2002, pp. 733-741.

[18] RTCA Special Committee 159, "Minimum Operational Performance Standards for Global Positioning System/Wide Area Augmentation System Airborne Equipment," Document No. RTCA/DO-229C, Washington, DC, 2001.

[19] G. McGraw, T. Murphy, M. Brenner, S. Pullen, and A. Van Dierendonck, "Development of the LAAS Accuracy Models," *Proc. ION GPS*, Salt Lake City, UT, 2000, pp. 1212-1223.

[20] B. Pervan, "Navigation integrity for aircraft precision landing using the Global Positioning System," PhD Dissertation, Stanford University, Stanford, CA, 1996.